nature geoscience

Article https://doi.org/10.1038/s41561-023-01348-3

Coevolving aerodynamic and impact ripples on Earth

In the format provided by the authors and unedited

Contents

SUPPLEMENTARY METHODS

S1 Grain-scale numerical simulation

To simulate impact ripple formation under diverse transport conditions, and determine relevant transport quantities for our ambient-air conditions, we use the numerical model of Durán et al.[1], which couples a discrete element method for the particle motion under gravity, buoyancy, and fluid drag with a continuum Reynolds-averaged description of hydrodynamics. The simulations reproduce measurements of the rate and threshold of aeolian transport, and viscous and turbulent subaqueous transport (Figs. 1 and 3 of Pähtz and Durán[2] and Fig. 4 of Pähtz and Durán[3]), and height profiles of relevant equilibrium transport properties (Fig. 2 of Pähtz and Durán[2] and Fig. 6 of Durán et al.[4]). Spherical particles ($\sim 10^4$) with mild polydispersity are confined in a quasi-two-dimensional domain of length $\sim 10^3 d$ (where d is the mean particle diameter) and open height, with periodic boundary conditions in the flow direction. The bottom-most particle layer is glued on a bottom wall, while the top of the simulation domain is reflective but so high that it is never reached by transported particles. The fluid, characterized by a density ρ_f and a kinematic viscosity ν, is set into motion by a turbulent shear stress $\tau \equiv \rho_f u_*^2$ imposed far above the bed. The grains, of density ρ_p, are subject to gravity g and interact through repulsive contact forces. There is a grain-fluid two-way coupling via drag and buoyancy forces, incorporated at the discrete level in the equations of motion of the grains, and, at the continuum level, via a body force term in the Reynolds-averaged Navier-Stokes equations. The latter are combined with a semiempirical mixing length closure that ensures a smooth hydrodynamic transition from high to low particle concentration at the bed surface and quantitatively reproduces the mean turbulent flow velocity profile for a flat bed in the absence of transport. In this approach, flow pertubations in the streamwise direction resulting from pertubations of the flat-bed topography are averaged out, implying that the model is, by construction, unable to reproduce bedform formation due to hydrodynamic instabilities. The control parameters of the model are the density ratio $s \equiv \rho_p/\rho_f$, the Galileo number

$\mathrm{Ga} \equiv \sqrt{(s-1)gd}d/\nu$, and the Shields number $\Theta \equiv u_*^2/((s-1)gd)$.

To facilitate the comparison with the wind tunnel experiments, we run the simulation with the parameters corresponding to our ambient-air conditions ($s = 2083$ and $\mathrm{Ga} = 8.1$) for diverse Shields numbers. For the environmental conditions pertaining to the ambient-air wind tunnel experiments ($\Theta = 0.0184$), we obtain the sand flux $q_0 \approx 2.1\ \mathrm{g/(ms)}$ above the bed surface and vertical flux $\varphi \approx 0.26\ \mathrm{kg/(m^2s)}$ at the bed surface, from the simulations. Furthermore, we compute the average hop length as $\bar{\ell}_{\mathrm{hop}} = q_0/\varphi$[5], which gives the value $\bar{\ell}_{\mathrm{hop}} \approx 7.7 \pm 0.3\ \mathrm{mm} \approx 85d$.

S2 Theory behind the estimation of the saturation length

In unidirectional sand transport, the saturation length ℓ_{sat} characterizes the relaxation length of the perturbed sand flux $q(x,t)$ towards its equilibrium value, the saturated sand flux $q_s(x,t)$, such that, near saturated conditions, in a first approximation the sand flux follow the relaxation equation[6–8]

$$\frac{\partial q}{\partial x} = \frac{q_s - q}{\ell_{\mathrm{sat}}}, \tag{S1}$$

where the saturated sand flux $q_s \propto \tau$ is proportional to the bed shear stress, which is in turn a functional of the surface elevation $h(x,t)$. Following mass conservation (Exner equation) under conditions of approximate lateral uniformity ($\partial q/\partial y = 0$),

$$\frac{\partial h}{\partial t} = -\phi_b^{-1}\frac{\partial q}{\partial x}, \tag{S2}$$

bedforms can emerge under suitable conditions (ϕ_b is the bed volume fraction). Using linear stability analysis, it can be shown that, during the initial phase of bedform growth, a low-amplitude sinusoidal signal forms at a given wavelength λ (the initial bedform wavelength or size), which is a function of the saturation length ℓ_{sat} and the details of how the bed shear stress changes in response to the topography[6,7,9]. At this initial stage, both the sand flux and bed shear stress perturbation are also sinusoidal with the same wavelength λ and very small amplitudes. Therefore, the flux relaxation equation implies

$$q(x,t)(1+ik\ell_{\text{sat}}) = q_s(x,t) \propto \tau(x,t), \tag{S3}$$

with $k = 2\pi/\lambda$. For wavelengths much larger than the saturation length, $1 + ik\ell_{\text{sat}} \approx e^{ik\ell_{\text{sat}}}$, and thus

$$q(x,t) \propto \tau(x,t)e^{-ik\ell_{\text{sat}}}, \tag{S4}$$

which means the flux is shifted downstream relative to the bed shear stress by $k\ell_{\text{sat}}$ and suggests that the saturation length can be estimated from the phase lag between sand flux and bed-shear-stress perturbation during the initial stages of the bedform formation (cf. Fig. 3 of the main text).

SUPPLEMENTARY FIGURES

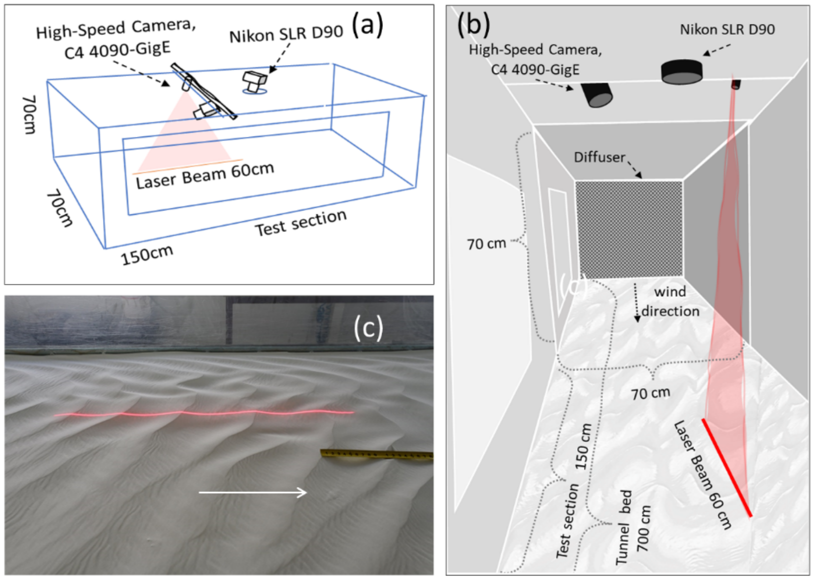

Figure S1: **Ambient-air wind tunnel.** Sketch of side (a) and front (b) view of the ambient-air wind tunnel at Ben-Gurion University. The laser module, 3D camera, and Nikon D-90 were installed in the tunnel roof for documentation of ripple morphology. (c) Exemplary side view of ripples evolving in the wind tunnel.

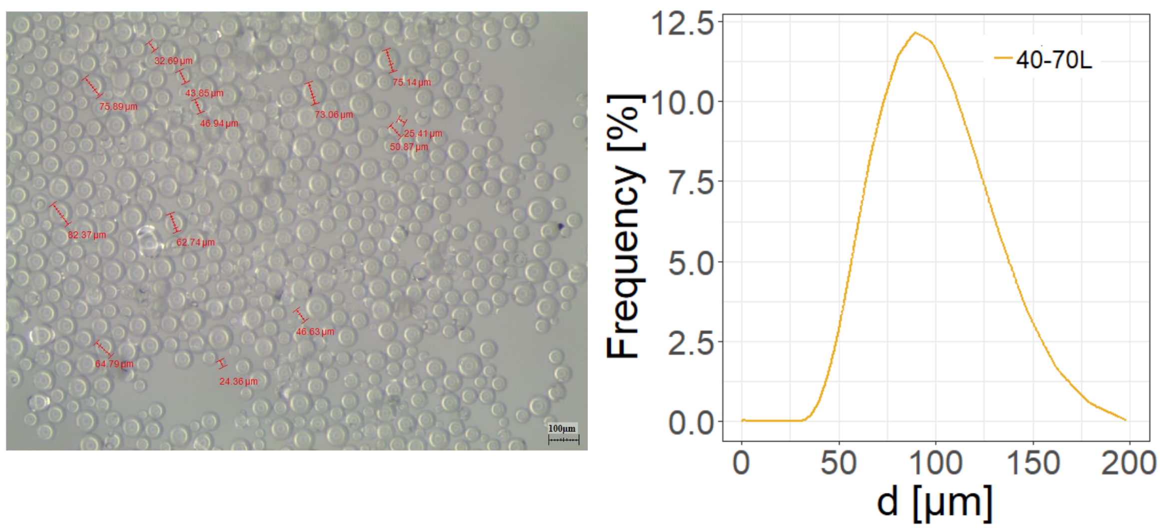

Figure S2: **Sand source.** Micrograph and grain size distribution of the glass beads (purchased from the German company "Kuhmichel" (`https://www.kuhmichel.com/en/products/glass-beads/`)) of density $\rho_p = 2500\,\mathrm{kg/m^3}$, used both in the ambient-air and the low-pressure wind tunnel; digital image taken through a microscope (left) and grain size distribution (right) show a mean diameter $d \approx 90 \pm 35\ \mu$m. Grain size distribution was analyzed by a high-resolution laser diffractometer[10] covering the grain-size range $0.04\,\mu\mathrm{m}$ to $1924\,\mu\mathrm{m}$ with a resolution of 102 bins of increasing width Δd from $\Delta d = 0.05\,\mu\mathrm{m}$ in the very fine fraction to $\Delta d = 183\,\mu\mathrm{m}$ in the very coarse fraction.

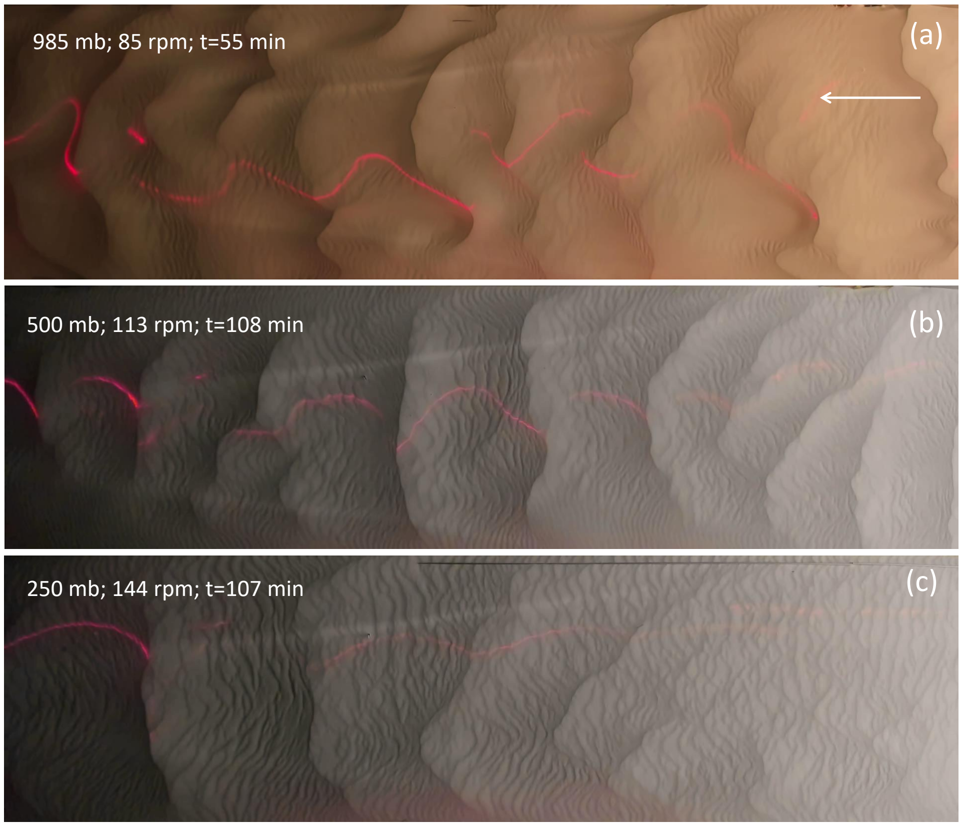

Figure S3: **Low-pressure wind tunnel experiments.** Examples of top-view photos taken in the pressure-controlled wind tunnel at Aarhus University (AWTSII), which are used to infer the wavelengths of small and large ripples using a digital image correlation technique[11] (Methods and Fig. S8). The coexistence of both ripple types was found for $P = [985, 500, 250]$ mb, while for $P = [100, 16]$ mb only one type of bedform (presumably impact ripples) could be observed during the total duration of 3.5 h.

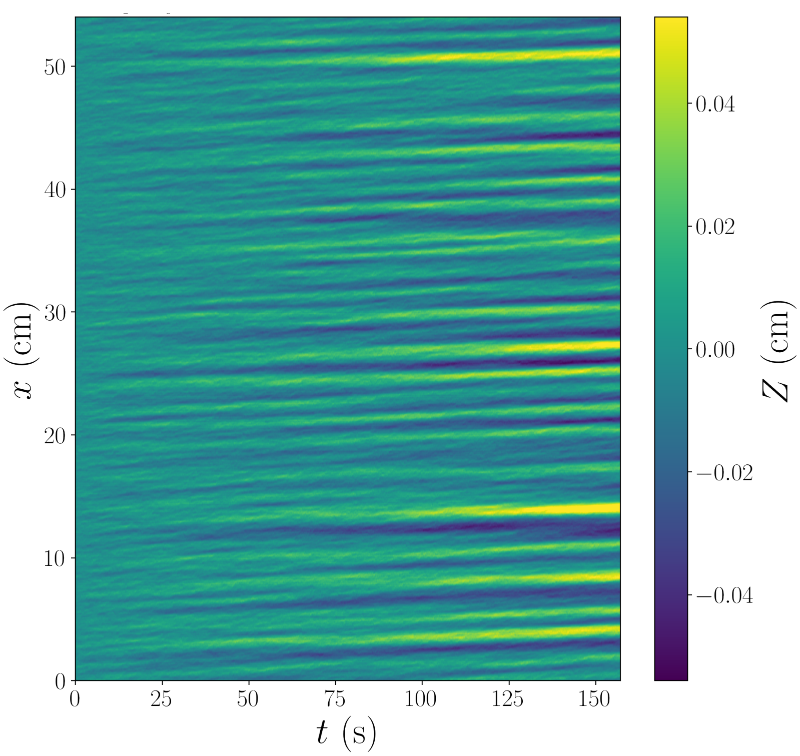

Figure S4: **Numerical simulation of the formation of impact ripples.** Spatio-temporal plot of the formation of impact ripples, for conditions mimicking those of our ambient-air wind tunnel experiments: grain size $d = 90$ μm, wind shear velocity $u_* = 0.18$ m/s, and grain-fluid density ratio $\rho_p/\rho_f = 2083$.

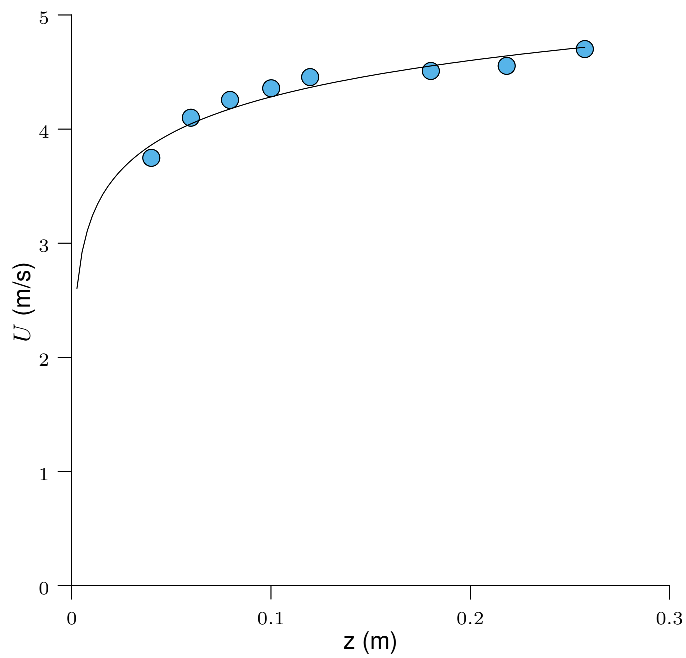

Figure S5: **Ambient-air wind tunnel – wind velocity.** Measured wind speed profile fitted by the standard log-profile $U(z) = u_*/\kappa \ln(z/z_0)$ for the hydrodynamically smooth regime with roughness length $z_0 = 0.11\nu/u_*$, where $\kappa = 0.4$, ν is the kinematic viscosity and $u_* = 0.184 \pm 0.03$ m/s.

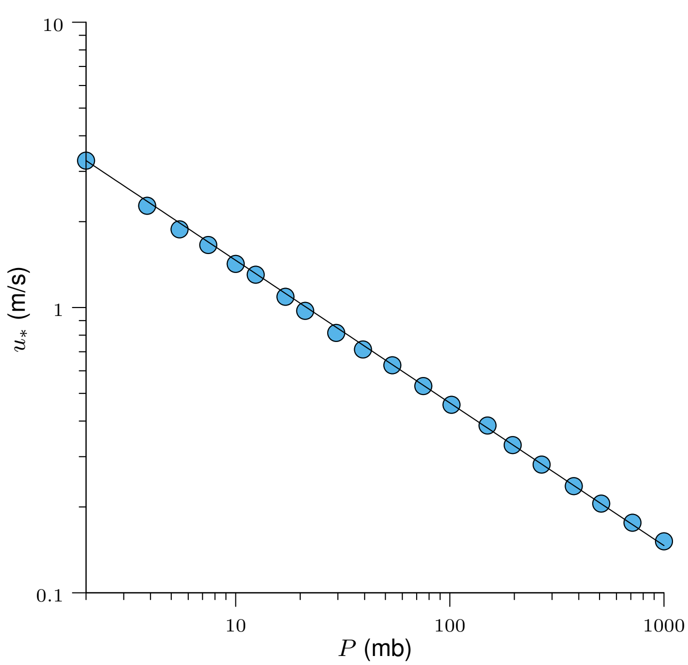

Figure S6: **Low-pressure wind tunnel – friction velocity.** Measured wind shear velocity u_* for different pressures P. The fit corresponds to the relation $u_* = \sqrt{(0.0117 \pm 10^{-6})(\rho_p/\rho_f - 1)gd}$.

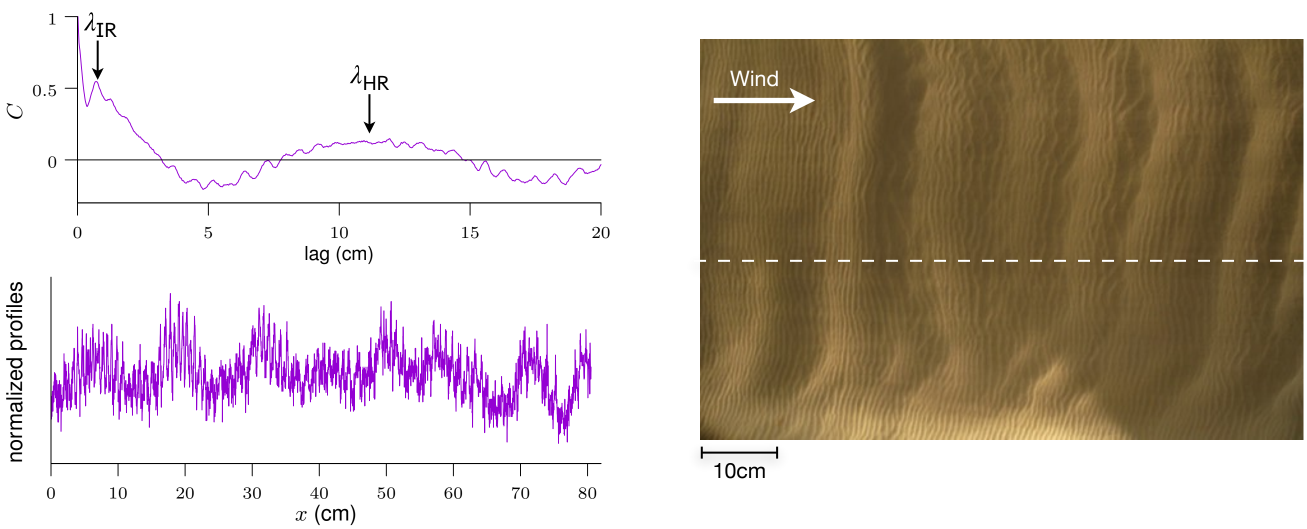

Figure S7: **Bedform wavelengths from ambient-air wind tunnel top-view photos.** Estimation of the wavelength of both small and large ripples using the autocorrelation function Eq. M1 (top left) of the pixel intensity profile $\eta(x)$ (bottom left) along a transect on the top-view photo of the bed shown on the right. Pixel intensity is defined as the average of the RGB channels.

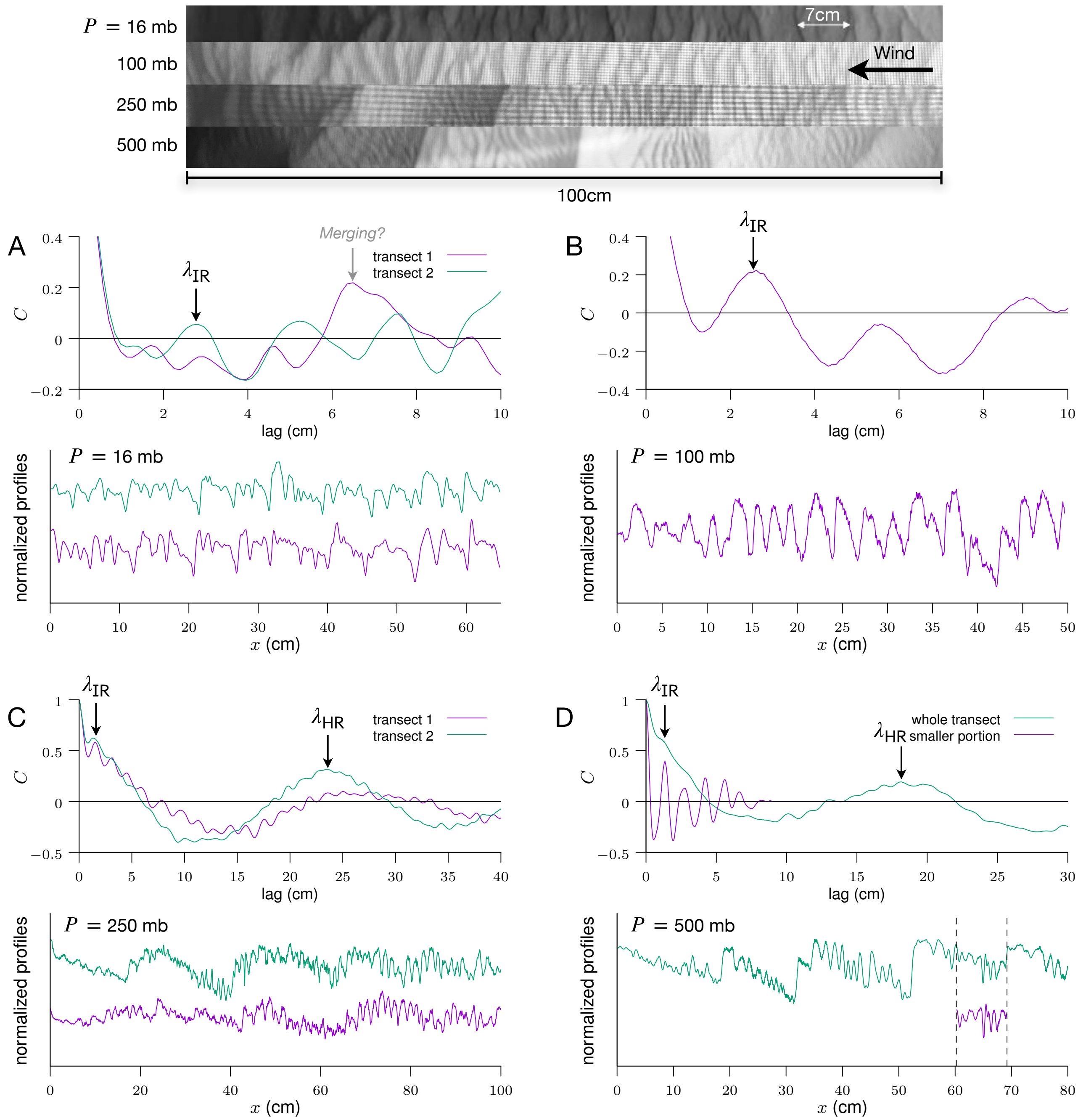

Figure S8: **Bedform wavelengths from low-pressure wind tunnel top-view photos.** (A-D) Estimation of the wavelength of both small and large ripples (when present) using the autocorrelation function Eq. M1 (top panels) of the pixel intensity profile $\eta(x)$ (bottom panels) along a transect on a top-view photo of the bed (top panel) for various pressures: 16 mb (A), 100 mb (B), 250 mb (C) and 500 mb (D). See Methods for further details.

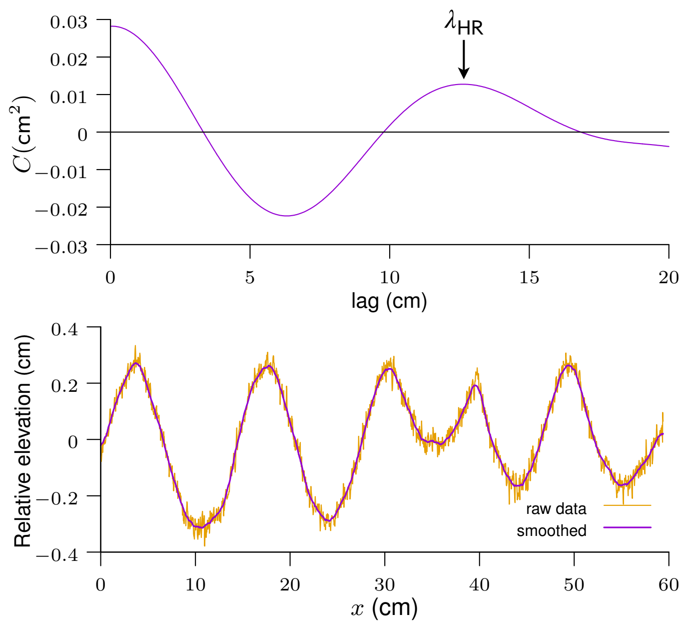

Figure S9: **Bedform wavelength and amplitude from ambient-air wind tunnel bed elevation data.** Estimation of ripple wavelength and amplitude using the autocorrelation function Eq. M2 (top) of the bed elevation profile $h(x)$ (bottom), captured by a laser sheet. Elevation data is smoothed to reduce the noise due to the poorly captured impact ripples. See Methods for details.

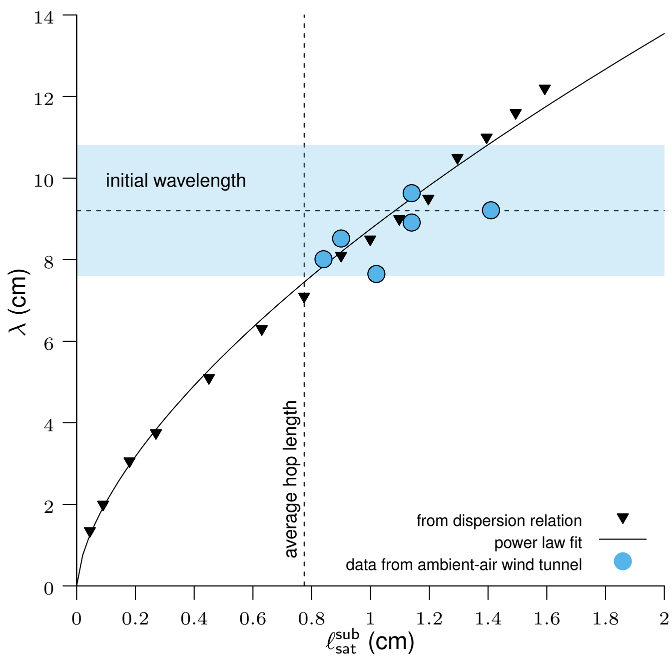

Figure S10: **Hydrodynamic model validation.** Fastest growing wavelength λ ($\triangledown$) from the dispersion relation as function of the subscale saturation lengths $\ell_{\text{sat}}^{\text{sub}}$ for the parameters of the ambient-air wind tunnel experiment. The line is the power-law fit, $\lambda = 50 d_\nu (\ell_{\text{sat}}^{\text{sub}}/d_\nu)^{0.63}$, with the viscous length $d_\nu = \nu/u_* = 81\ \mu\text{m}$. Circles represent measured wavelength and subscale saturation length every minute from 9 to 14 min, within the linear instability regime. The wavelength is estimated from top-view photos and averaged over a minute (i.e. 5 photo taken every 20 s), whereas the corresponding $\ell_{\text{sat}}^{\text{sub}}$ is estimated from the elevation profile (measured every minute), as explained in the Methods. The average (dashed line) and standard deviation (shaded area) of the initial wavelength (for $t < 15$min) is also shown for comparison, as well as the average hop length estimated from grain-scale simulations (Supplementary Methods).

SUPPLEMENTARY TABLES

ρ_p/ρ_f	d [μm]	u_* [m/s]	ν/u_* [μm]	λ_{IR} [cm]	λ_{HR} [cm]	$\lambda_{\mathrm{HR}}^{\mathrm{init}}$ [cm]	σ_{HR} [min^{-1}]
$2,083$	90 ± 35	0.184 ± 0.003	81 ± 1.3	0.8 ± 0.1	12.8 ± 2.4	9.2 ± 1.6	0.180 ± 0.005

Table S1: **Ambient-air wind tunnel data.** Particle-fluid density ratio ρ_p/ρ_f; mean grain diameter d; wind friction velocity u_* estimated from wind profile (Methods); viscous sublayer scale ν/u_*; wavelength of impact (λ_{IR}) and aerodynamic (λ_{HR}) ripples estimated from top-view photos (mean and standard deviation over the whole experiment, see Fig. 2b and Methods); initial wavelength of aerodynamic ripples ($\lambda_{\mathrm{HR}}^{\mathrm{init}}$, mean and standard deviation) calculated from top-view photos in the first 15 minutes, within the linear instability regime; and growth rate σ_{HR} of aerodynamic ripples estimated from the time series of the ripple amplitude (Methods); λ_{IR}, λ_{HR} and ν/u_* are shown in Fig. 1f, whereas σ_{HR} and $\lambda_{\mathrm{HR}}^{\mathrm{init}}$ are used in Fig. 4.

P [mb]	ρ_p/ρ_f	d [μm]	u_* [m/s]	ν/u_* [μm]	λ_{IR} [cm]	λ_{HR} [cm]
500	$4,166$	90 ± 35	0.206 ± 0.002	146 ± 4	1.5 ± 0.5	18.2 ± 0.6
250	$8,332$	90 ± 35	0.286 ± 0.003	208 ± 6	1.6 ± 0.3	19.8 ± 3.3
100	$20,830$	90 ± 35	0.452 ± 0.004	332 ± 10	2.5 ± 0.2	—
16	$130,187$	90 ± 35	1.11 ± 0.01	844 ± 25	2.8 ± 0.7	—

Table S2: **Low-pressure wind tunnel data.** Wavelengths λ_{IR} and λ_{HR} of small and large ripples, respectively, estimated from top-view photos (Methods) and the parameters (pressure P, wind friction velocity u_* and particle-fluid density ratio ρ_p/ρ_f) used for the calculation of the viscous length ν/u_* as shown in Fig. 1f of the main text.

ρ_p/ρ_f	d [μm]	u_* [m/s]	ν/u_* [μm]	$\lambda_{\mathrm{IR}}^{\mathrm{init}}$ [cm]
$2,000$	64	0.14	101	1.2 ± 0.4
$2,000$	64	0.18	81	1.1 ± 0.3
$2,000$	102	0.13	107	1.8 ± 0.5
$2,083$	90	0.19	80	1.5 ± 0.4
$2,083$	90	0.22	69	1.7 ± 0.5
$10,000$	124	0.29	251	2.1 ± 0.6
$50,000$	102	0.62	578	2.8 ± 0.8
$100,000$	128	0.74	969	3.9 ± 1.2

Table S3: **Impact ripples from grain-scale numerical simulations.** Particle-fluid density ratio ρ_p/ρ_f, grain size d, wind friction velocity u_*, viscous sublayer scale ν/u_*, and initial wavelengths $\lambda_{\mathrm{IR}}^{\mathrm{init}}$ of simulated impact ripples, shown in Fig. 1f of the main text. In the simulations we consider terrestrial conditions: gravity acceleration $g = 9.8\ \mathrm{m/s^2}$ and air dynamic viscosity $\mu = \nu\rho_f = 1.8 \times 10^{-5}\ \mathrm{kg/(ms)}$.

ρ_p/ρ_f	d [μm]	u_* [m/s]	u_t [m/s]	q_0/ρ_p [m^2/yr]	ℓ_{sat} [m]	λ_D [m]	σ_D [yr^{-1}]	σ_D^+
$1,976$	190	0.29	0.19	18.4	0.95 ± 0.2	16.5 ± 2.0	1.8	1.2×10^{-9}

Table S4: **Field measurement data for incipient dunes on Earth by Lü et al. (2021)[12].** Incipient dunes' wavelength λ_D, growth rate σ_D, grain size d, wind friction velocity u_*, grain entrainment threshold friction velocity u_t, total sand flux q_0, divided by grain density ρ_p, and saturation length ℓ_{sat}. The dimensionless growth rate, defined as $\sigma_D^+ = \sigma_D\, \phi_b \rho_p [1 - (u_t/u_*)^2] d^2/q_0$ (Methods), with bed volume fraction $\phi_b = 0.6$, is used for the validation of the dispersion relation shown in Fig. 4 of the main text.

Run type	Dunes[a]	Dunes[b]	Ripples & Dunes[b]
weight of subscale modulation γ	0	0	0.1
density ratio ρ_p/ρ_f	$1,976$	$2,083$	$2,083$
grain size d [μm]	190	90	90
wind shear velocity u_* [m/s]	0.29	0.184	0.184
threshold shear velocity u_t [m/s]	0.19	0.135^c	0.135^c
volumetric saturated flux* [c] q_0/ρ_p [m^2/yr]	69	17	17
subscale saturation length[d] $\ell_{\mathrm{sat}}^{\mathrm{sub}} = \bar{\ell}_{\mathrm{hop}}$ [m]	—	—	$(7.7 \pm 0.3) \times 10^{-3}$
saturation length[13] $\ell_{\mathrm{sat}} = 4500d$ [m]	0.86	0.41	0.41
Model predictions			
initial wavelength of hydro-ripples λ_{HR} [m]	—	—	$(7.1 \pm 0.1) \times 10^{-2}$
ripple growth rate* σ_{HR} [min^{-1}]	—	—	0.18
dimensionless ripple growth rate σ_{HR}^+	—	—	1.31×10^{-5}
initial wavelength of dunes λ_D [m]	18.2	17.2	16.3
dune growth rate* σ_D [yr^{-1}]	6.8	2.77	3.30
dimensionless dune growth rate σ_D^+	1.18×10^{-9}	3.44×10^{-10}	4.1×10^{-10}

(^{a}) For conditions as measured in the field by Lü et al. (2021)[12].

(^{b}) For conditions as measured in our ambient-air wind tunnel.

(*) Under constant wind velocity.

(^{c}) Estimated using the threshold and sediment transport formulation in Pähtz and Duran[14].

(^{d}) Estimated from grain-based numerical simulations.

Table S5: **Model parameters and predictions.** Parameters and predictions for the three different calculations of the dispersion relation shown in Fig. 4.

1. Durán, O., Andreotti, B. & Claudin, P. Numerical simulation of turbulent sediment transport, from bed load to saltation. Physics of Fluids **24**, 103306 (2012).

2. Pähtz, T. & Durán, O. The cessation threshold of nonsuspended sediment transport across aeolian and fluvial environments. Journal of Geophysical Research: Earth Surface **123**, 1638–1666 (2018).

3. Pähtz, T. & Durán, O. Unification of aeolian and fluvial sediment transport rate from granular physics. Physical Review Letters **124**, 168001 (2020).

4. Durán, O., Andreotti, B. & Claudin, P. Turbulent and viscous sediment transport - a numerical study. Advances in Geosciences **37**, 73–80 (2014).

5. Durán, O., Claudin, P. & Andreotti, B. On aeolian transport: Grain-scale interactions, dynamical mechanisms and scaling laws. Aeolian Research **3**, 243–270 (2011).

6. Andreotti, B., Claudin, P. & Douady, S. Selection of dune shapes and velocities part 2: A two-dimensional modelling. The European Physical Journal B **28**, 341–352 (2002).

7. Kroy, K., Sauermann, G. & Herrmann, H. J. Minimal model for aeolian sand dunes. Physical Review E **66**, 031302 (2002).

8. Sauermann, G., Kroy, K. & Herrmann, H. J. A continuum saltation model for sand dunes. Physical Review E **64**, 031305 (2001).

9. Durán Vinent, O., Andreotti, B., Claudin, P. & Winter, C. A unified model of ripples and dunes in water and planetary environments. Nature Geoscience **12**, 345–350 (2019).

10. Katra, I. & Yizhaq, H. Intensity and degree of segregation in bimodal and multimodal grain size distributions. Aeolian Research **27**, 23–34 (2017).

11. Andreotti, B., Fourrière, A., Ould-Kaddour, F., Murray, B. & Claudin, P. Giant aeolian dune size determined by the average depth of the atmospheric boundary layer. Nature **457**, 1120–1123 (2009).

12. Lü, P. et al. Direct validation of dune instability theory. Proceedings of the National Academy of Sciences **118**, e2024105118 (2021).

13. Andreotti, B., Claudin, P. & Pouliquen, O. Measurements of the aeolian sand transport saturation length. Geomorphology **123**, 343–348 (2010).

14. Pähtz, T. et al. Unified model of sediment transport threshold and rate across weak and intense subaqueous bedload, windblown sand, and windblown snow. Journal of Geophysical Research: Earth Surface **126**, e2020JF005859 (2021).